

Spin purity of the quantum dot confined electron and hole in an external magnetic fieldDan Cogan , Zu-En Su, Oded Kenneth, and David Gershoni ^{*}*The Physics Department and the Solid State Institute, Technion–Israel Institute of Technology, Haifa 3200003, Israel*

(Received 30 August 2021; revised 2 January 2022; accepted 5 January 2022; published 14 January 2022)

We investigate experimentally and theoretically the temporal evolution of the spin of the conduction band electron and that of the valence band heavy hole, both confined in the same semiconductor quantum dot. We use all-optical pulse techniques to perform complete tomographic measurements of the spin as a function of time after its initialization and study the total spin purity (coherence), measured here. In the important limit of a weak externally applied magnetic field, comparable in strength to the Overhauser field due to fluctuations in the surrounding nuclei spins, the measured spin purity performs complex temporal oscillations. We use a central-spin model encompassing the spin's Zeeman and the hyperfine interactions to reproduce the measured results quantitatively. Our studies are essential for designing and optimizing quantum-dot-spin-based entangled multiphoton sources that set stringent limitations on the magnitude of the externally applied field.

DOI: [10.1103/PhysRevB.105.L041407](https://doi.org/10.1103/PhysRevB.105.L041407)

Semiconductor quantum-dot-based devices are currently the most viable technology for generating quantum light for future quantum information and network applications. They are easily incorporated into electro-optical classical components [1–5] while demonstrating unparalleled efficiency, photon extraction rates [4–6], and high quality, nearly transform-limited photon indistinguishability [5–8]. Furthermore, a quantum dot (QD) acts as a single atom emitter and thus can be a source of entangled photon pairs via its spontaneous emission [4,9,10]. Spin-photon entanglement, achieved via optical recombination of an excited QD confined charged spin [11–13], has been proposed for many quantum technological applications [14]. Most relevant for this study is the demonstrated proposal to use a QD confined spin as an entangler for generating multiphotonic entangled graph and cluster states [15–18]. These photonic states are essential resources for quantum communication and entanglement distribution between remote nodes [19–22]. An essential requirement for these applications is a long spin coherence time. In addition, spin-based quantum technologies often use an external magnetic field to lift the spin degeneracy [23] and induce coherent spin precession via the Zeeman interaction. Spin-photon entanglement requires that the precession period, which is inversely proportional to the magnitude of the external field, be much longer than the radiative lifetime of the emitted photon. This requirement therefore severely limits the magnitude of the externally applied field. It therefore follows that understanding a QD confined spin's decoherence mechanisms in the presence of external magnetic fields is interesting and important both scientifically and technologically. For entangled light generation, relatively weak fields are particularly important [18].

The primary decoherence mechanism of electronic spin qubits in QDs is the hyperfine interaction with the $\sim 10^5$

nuclei's spin in the QD [24–27]. Local fluctuations in the nuclear spin polarization generate an effective magnetic (Overhauser) field that the spin interacts with. The random statistical nature of this field is the main reason for the spin coherence loss. We define the hyperfine interaction parameters in energy units as the averaged interaction of the electronic spin with the ensemble of nuclear spins in the QD [28,29]. While the conduction-electron interaction with the nuclear spin, which we denote by γ_e , is mostly isotropic [25], the interaction of the valence heavy hole (HH) (a hole with parallel orbital momentum and spin) is anisotropic [27]. We denote by γ_{h_z} (γ_{h_p}) the HH's hyperfine interaction parameter along (perpendicular to) the QD's growth axis \hat{z} [28].

In this Letter, we study experimentally and theoretically the decoherence mechanism of both the QD confined electron [30,31] and HH [32–38] spins in the presence of externally applied magnetic fields and the statistical Overhauser field. We provide a comprehensive description of both carriers' spin decoherence processes by accurately mapping the total spin purity evolution dependence on the externally applied field magnitude from zero [28,39] to strong fields [30,31] relative to the Overhauser field. It turns out that the field magnitude in which spin-photon entanglement prevails, the Zeeman interaction, is comparable in magnitude to the hyperfine interaction with the Overhauser field. Thus, one must consider both interactions in designing QD-based devices for entangled light sources [18]. We set the external magnetic field B_{ext} in the x direction, initialize the central spin in the z direction, and measure the complex oscillations in the coherence. We show that they depend on the ratio between the magnetically induced Zeeman interaction and the hyperfine interaction perpendicular to x , defined by

$$r = C_{\text{Zeeman}}/C_{\text{hf}}^{\perp} = \frac{g_x \mu_B B_{\text{ext}}}{\sqrt{\gamma_y^2 + \gamma_z^2}}. \quad (1)$$

^{*}dg@physics.technion.ac.il

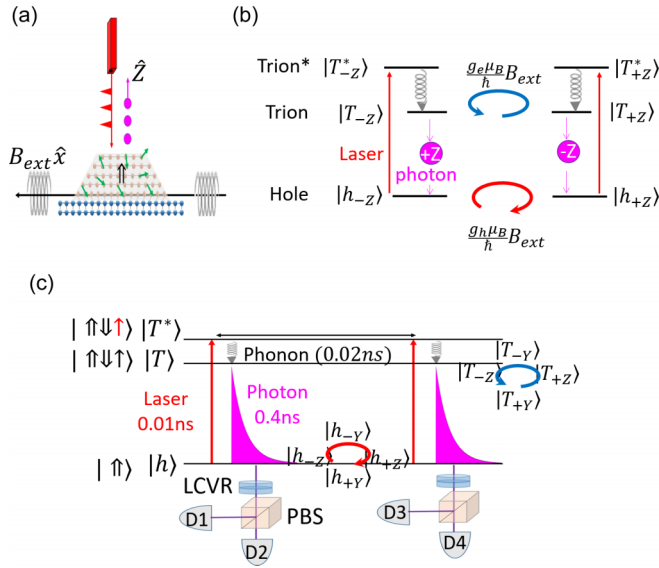


FIG. 1. (a) The QD sample. The 12-ps laser π pulses (marked in red) resonantly excite the central spin. The excited spin then returns to its ground state by emitting single photons (pink circles). The spin evolves under the joint influence of the external and nuclear magnetic fields. Green arrows represent the randomly distributed nuclear spins. (b) The polarization selection rules for the hole-trion optical transition. $\pm Z$ is the polarization of the exciting laser and the emitted photons. (c) The experimental setup for initializing and probing the central-spin evolution. Liquid-crystal variable retarders (LCVRs) and polarizing beam splitters (PBSs) are used to project the photon polarization. By selecting the polarization of the exciting pulses and that of the projected photons, while setting the time difference between the pulses, one can fully investigate the electron and hole spin evolution.

Here, g_x is the central spin's Landé factor along the x direction, γ_y and γ_z are the hyperfine parameters along the y and z directions [28], and μ_B is the electron Bohr magneton. We compare the measured results to a central-spin model encompassing the Zeeman and hyperfine interactions [29].

We mark the HH spin along the shortest axis of the QD's three-dimensional (3D) potential trap [marked $+Z$ in Fig. 1(a)] by $|\uparrow\rangle$ ($|\downarrow\rangle$) for the spin-up (spin-down) state. A resonantly tuned laser pulse photogenerates an extra electron-hole pair in the QD, converting the HH to a positive trion ($|\uparrow\downarrow\uparrow\rangle$). The ground level of the positive trion is composed of two paired HHs with opposite spins and a single conduction band electron. The selection rules for optical transitions between the HH spin states and that of the trion form a π system [28] with the following optical transitions:

$$\begin{aligned} |\uparrow\rangle &\xleftrightarrow{|-Z\rangle} |\uparrow\downarrow\uparrow\rangle, \\ |\downarrow\rangle &\xleftrightarrow{|+Z\rangle} |\downarrow\uparrow\downarrow\rangle, \end{aligned} \quad (2)$$

where $|+Z\rangle$ and $|-Z\rangle$ denote the right- and left-hand circular polarization states of the photon inducing the optical transition between the ground level qubit (HH) and the excited qubit (trion), as described in Fig. 1(b).

We note that this system allows us to investigate both the valence band HH and the conduction band electron as

TABLE I. The QD g tensor and hyperfine-tensor components. Here, γ_{hp} , γ_{hz} , and γ_e are the interaction energies of the hole and electron spins with the nuclear spin environment and g_h^x and g_e^x are the relevant HH and electron g -tensor components. The positive trion radiative time is τ_{photon} .

	This work	Literature
γ_{hp}	$0.029 \pm 0.005 \mu\text{eV}$	0.031 [28], 0.047 [34]
γ_{hz}	$0.12 \pm 0.02 \mu\text{eV}$	0.11 [28], 0.081 [34]
γ_e	$0.693 \pm 0.006 \mu\text{eV}$	0.34 [28], 0.33 [39]
g_h	-0.128 ± 0.002	
g_e	0.367 ± 0.004	
τ_{photon}	$0.398 \pm 0.004 \text{ ns}$	

central spins. The HH is investigated through the ground level qubit while the electron through the excited level trion. The interaction for the paired HH spins vanishes, leaving only the electron to consider [28].

Figures 1(a) and 1(b) show a schematic description of the InAs in a GaAs self-assembled QD sample and the polarization selection rules for the hole-trion optical transition, respectively. The strained QD single layer was grown on a (001)-oriented GaAs substrate, embedded in a one wavelength planar microcavity formed by two Bragg reflecting mirrors [17]. The QD charge is statistically controlled using a very weak above-band-gap laser excitation [28]. Detecting a photon from the X^{+1} optical transition heralds the HH in the QD. The externally applied in-plane magnetic field induces coherent evolution of the central spins, which precess between their spin-up and spin-down states. The interaction of the electronic spin with the nuclear spin environment inflicts decoherence on the evolving central spins.

We use two laser pulses to initialize and to probe the HH and the trion qubits as described in Fig. 1(c). Each laser pulse excites the HH to an excited-positive-trion level, where the unpaired electron is in its respective second energy level. We identify the absorption resonances of this QD for various charge states using PL excitation (PLE) spectroscopy as described elsewhere [41]. The energy separation between the excited and ground level of the electron almost resonates with the material's optical phonon. As a result, the relaxation of the excited electron is relatively fast (~ 20 ps) [41]. Since phonons very weakly interact with the electronic spin degree of freedom, the spin-phonon coupling times are orders of magnitude longer than the optical phonon-assisted relaxation. Thereby, the relaxation is spin preserving [41,42]. The trion then decays radiatively by emitting a photon within about 400 ps. We project the photon's polarization using pairs of liquid-crystal variable retarders (LCVRs) followed by polarizing beam splitters (PBSs), transmission gratings for spectral filtering, and superconducting single-photon counters for detection. The overall system efficiency is about 1% and its temporal resolution is about 30 ps. We initialize the HH and trion spin qubits by controlling the polarization of the resonant laser pulses. At the same time we also probe the state of these qubits by measuring the polarization of the emitted photons.

Figure 2 describes how we measure the spin evolution of the positive trion. We initialize the trion qubit to spin-up

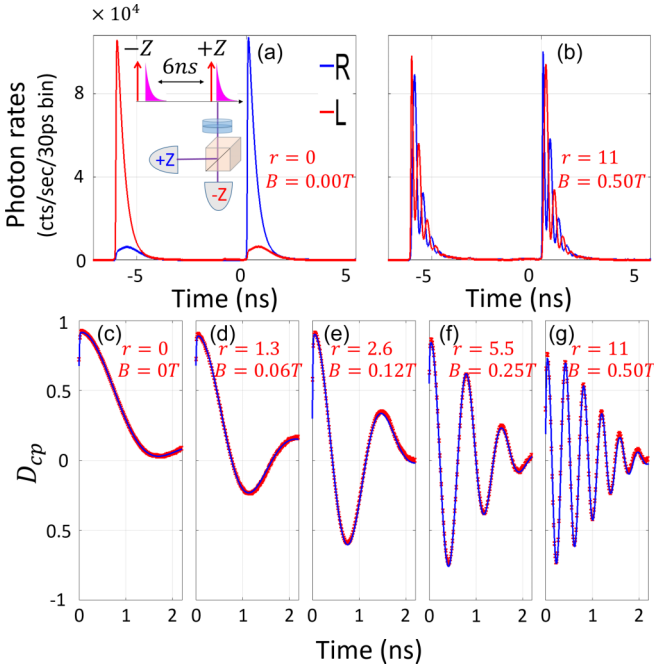


FIG. 2. Measurements of the trion spin evolution. Polarization-sensitive time-resolved photoluminescence (PL) emission from the positive trion transition for a Zeeman-hyperfine ratio [Eq. (1)] of (a) $r = 0$, and (b) $r = 11$. The inset in (a) describes the pulse (red arrows) and detection (magenta markings) sequence used for these measurements. The trion spin is alternately initialized to spin down and up to prevent buildup of the Overhauser field in the sample. (c)–(g) Time-resolved degree of circular polarization [D_{cp} , Eq. (3)] of the PL emission for various r parameters. Red marks represent the measured data and the overlaid blue lines represent our central-spin model best fits [29]. From these multiple fits, we deduce the electron’s g factor g_e , the interaction energy with the nuclear environment γ_e , and the trion’s radiative time τ_{photon} , as summarized in Table I.

and spin-down states alternately using $-Z$ and $+Z$ polarized 12-ps-long laser π pulses. This is done in order to avoid the accumulation of an unwanted Overhauser field [28,43–46]. We then monitor the spin evolution during the optical recombination by projecting the emitted photon on the $-Z$ and $+Z$ polarization basis. Figures 2(a) and 2(b) show the time-resolved PL emission of the emitted photons for $r = 0$ and $r = 11$, respectively. Since the trion in the $|T_{+z}\rangle$ state emits a $-Z$ photon while the $|T_{-z}\rangle$ state emits a $+Z$ photon, the spin evolution of the trion can be deduced from the polarization-sensitive time-resolved PL. For the Zeeman-hyperfine ratio $r = 11$ case [Eq. (1)], the trion’s spin precession around the external magnetic field is clearly visible, while for the $r = 0$ case, one can only observe the exponential radiative decay. To increase this measurement’s sensitivity, we look at the degree of circular polarization (D_{cp}) of the emission defined by

$$D_{cp}(t) = \frac{I_{+z}(t) - I_{-z}(t)}{I_{+z}(t) + I_{-z}(t)}, \quad (3)$$

where $I_{+z}(t)$ [$I_{-z}(t)$] denotes the measured polarized PL intensity. The $D_{cp}(t)$ distills the information on the spin evolution from the characteristic exponential radiative decay

[28,40]. Using Eq. (2), it is straightforward to show that the $D_{cp}(t)$ measures the trion’s spin projection on the Z axis, $S_z(t)$.

Figures 2(c)–2(g) show the measured $D_{cp}(t)$ for five different r cases. For $r = 0$, the spin polarization evolves only due to the hyperfine interaction. It first decays within ~ 1.65 ns and then revives back to 1/3 of its initial value [25,28,39]. For $r > 0$, the spin evolves around the vector sum of \vec{B}_{ext} and \vec{B}_N . One notes that the measured initial spin polarization is not perfect, e.g., even for $r = 0$, it deviates from 1. There are two contributions to this deviation: (a) the LCVR-based polarization analysis, and (b) our detectors’ finite temporal resolution (~ 30 ps). These contributions result in a measured initial spin polarization of $S_z(0) = 0.92$ [$S_z(0) = 0.71$] for $r = 0$ ($r = 11$).

In Figs. 3(e)–3(h) we similarly present the measured HH spin temporal evolution for four different r ratios. The hole state is initialized to the $-Z$ state by projecting the first photon on $+Z$ polarization. For measuring the HH spin state as a function of time after this initialization we utilize a measurement technique which provides a full tomography of the HH spin [40]. Figures 3(a)–3(d) demonstrate the application of this technique 1 ns after initialization. The evolving hole state is promoted to the trion state by a second 1-ns delayed π pulse, linearly polarized $+X$ (horizontal), and $+Y$ (diagonal). The $+X$ polarized pulse promotes an arbitrary hole spin state $\alpha|h_{+z}\rangle + \beta|h_{-z}\rangle$ to the trion state, $\alpha|T_{+z}\rangle + \beta|T_{-z}\rangle$, while the $+Y$ polarized pulse results in a $\alpha|T_{+z}\rangle + i\beta|T_{-z}\rangle$ trion. The D_{cp} of the emission as a function of time for both cases provides the means for a full tomography of the HH spin state at the second excitation pulse [40]. The tomography or the HH spin projections $S_x(t)$, $S_y(t)$, and $S_z(t)$, for $t = 1$ ns, can be quite faithfully extracted from the best fitted model calculations to the measured points in Figs. 3(a)–3(d). These fits are presented by the solid black lines overlaid on the experimental measurements.

In Figs. 3(e)–3(h), we present by red, green, and blue the measured $S_x(t)$, $S_y(t)$, and $S_z(t)$, respectively, for various r ratios. The black points represent the spin purity which we define as $|S| = \sqrt{S_x^2 + S_y^2 + S_z^2}$. The color matched solid lines represent the calculated values [29] using the parameters in Table I.

In Fig. 4 we present the model-calculated time-resolved purity of the electron [in Fig. 4(a)] and HH [in Fig. 4(b)] spins, for various Zeeman-hyperfine ratios r [see Eq. (1)]. The shaded areas represent one standard deviation of the model’s uncertainties in the measured Table I values. For $r = 0$, the spin depolarizes, reaches minimum, and then partially revives. Spin precession around the frozen fluctuation of the nuclear field adequately describes this observation [25,28,39]. Since we initialize the spin in the z direction, γ_x and γ_y are the only relevant hyperfine tensor components contributing to the central-spin depolarization. γ_z , in contrast, pins the spin to its initial direction. Consequently, the spin reaches minimum within $t_{\text{min}} = h/[2(\gamma_x + \gamma_y)]$, with h being the Planck constant. This time is given by the hyperfine-induced spin precession perpendicular to the initialization direction. In addition, the value that the purity reaches after the revival depends on the ratio between γ_z and $\gamma_x + \gamma_y + \gamma_z$. Since the hyperfine tensor is isotropic for the electron its purity revives to 1/3. On the other hand, the anisotropic HH revives to $\sim 2/3$.

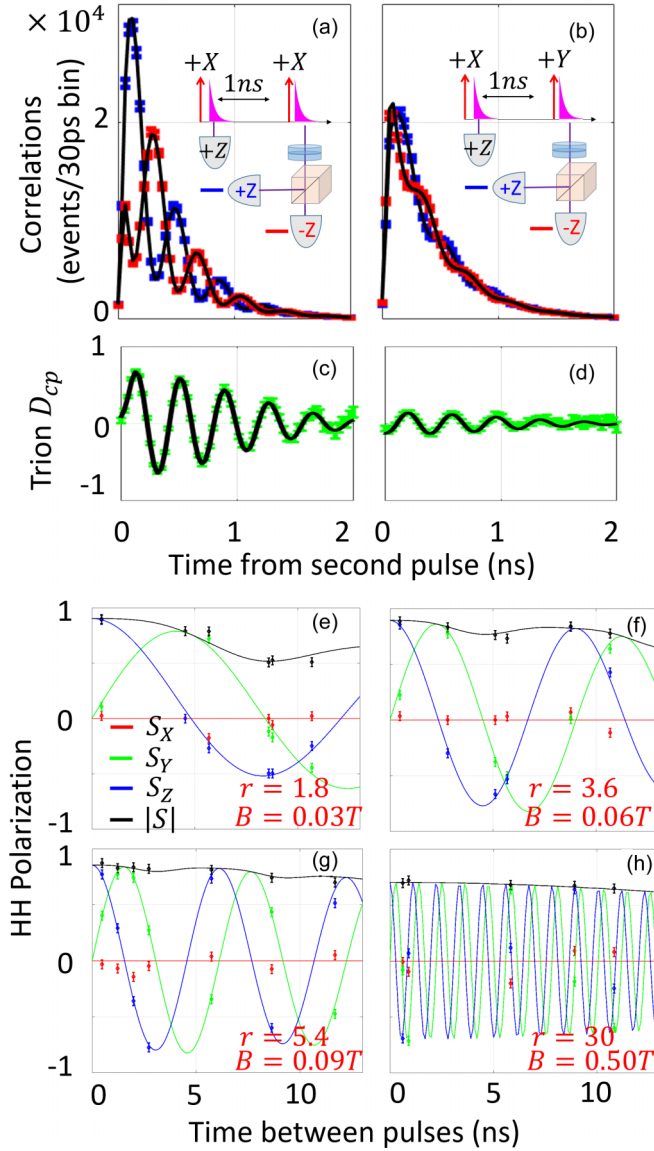


FIG. 3. The heavy-hole spin evolution. (a)–(d) Full tomography of the HH spin [40] at time $t = 1$ ns after its initialization to $+Z$ for a Zeeman-hyperfine ratio $r = 30$ [Eq. (1)]. (a) and (b) are polarization-sensitive time-resolved intensity correlation measurements of the trion emission after the second pulse. The insets describe the polarized pulse sequence (red arrows) and the resulting emission detection (magenta). (c) and (d) describe the degree of circular polarization [D_{cp} , see Eq. (3)] of the two-photon correlations, deduced from the measurements in (a) and (b), respectively. The black lines in (a)–(d) describe the best fitted model [see Supplemental Material (SM) [29]] from which the HH spin state [S_x, S_y, S_z] at the second pulse time is extracted [40]. Similar spin tomography measurements are performed for various pulse separation times (t) and for different ratios r . (e)–(h) Full tomography of the HH spin evolution is presented for various ratios r . The red, green, and blue marks describe the HH projections $S_x(t)$, $S_y(t)$, and $S_z(t)$, respectively, while the black marks describe the spin purity $|S| = \sqrt{S_x^2 + S_y^2 + S_z^2}$. The bars represent the measurement uncertainties and the color matched solid lines represent the model fit to the measured data [29]. From these fits, we extract the HH in-plane g factor g_h , and the hyperfine-interaction energies γ_{hp} and γ_{hc} (Table I).

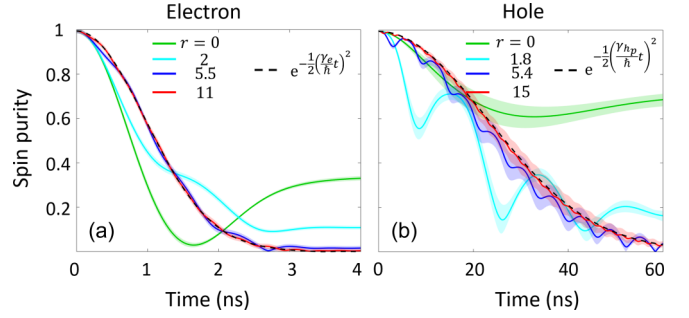


FIG. 4. Model calculated central-spin purity $|S(t)| = \sqrt{S_x^2(t) + S_y^2(t) + S_z^2(t)}$ vs time for (a) the electron, and (b) the heavy hole. The spin purity is calculated using the central-spin model (see SM and Table I). The spin is initialized in the z direction [$S_z(0) = 1$] and the external field is applied in the x direction. The colored lines represent the purity vs time from initialization for various Zeeman-hyperfine ratios r [Eq. (1)]. The shaded areas represent the uncertainties in the measured values of Table I. The calculations result from Fig. 2 for the electron and Fig. 3 for the hole. The dashed black line represents the analytic solution $|S(t)| = e^{-\frac{1}{2}(\frac{\gamma_h}{\hbar}t)^2}$ describing the purity in the limit $r \gg 1$, where the spin dephasing time $T_2^* = \sqrt{2\hbar/\gamma_x}$ is unambiguously defined. In the intermediate regime $r \sim 1$, T_2^* is not very well defined and can be regarded as the time it takes the spin purity to decay to 37% of its initial value.

For $r > 1$, as the external field increases, the Zeeman interaction becomes greater than the hyperfine interaction. The Zeeman-induced coherent spin precession averages the influence of the hyperfine interaction perpendicular to the field, effectively reducing γ_y and γ_z . This effect can be viewed as a natural dynamical decoupling. This in turn results in temporal oscillations of the central-spin purity. The frequency of these oscillations increases linearly with r while their amplitude decays. In addition, the spin revival peak reduces with the field as the effective ratio $\gamma_z/(\gamma_x + \gamma_y + \gamma_z)$ decreases. In the limit $r \gg 1$, the temporal dependence of the spin purity decay can be expressed analytically as $|S(t)| = e^{-\frac{1}{2}(\frac{\gamma_h}{\hbar}t)^2}$ depending only on the hyperfine interaction parallel to the field direction (see SM). Finally, we note that in Ref. [18], the HH spin was used as an entangler for the deterministic generation of a cluster state of entangled and indistinguishable photons. The optimal magnetic field found in Ref. [18] was 0.09 T ($r = 5.4$), indicating the significance of our Letter.

In summary, we present a comprehensive experimental and theoretical study of the central-spin coherence in the mutual influence of an external magnetic field and a statistical Overhauser field of comparable sizes. For the central spin, we consider the heavy-hole and electron spins, confined in the same QD. We perform complete tomographical measurements of the central spin and show that its purity (coherence) oscillates in time during its dephasing. The amplitude of these oscillations depends on the ratio between the external field and the statistical Overhauser field induced by the nuclei spin. For larger external fields, the central spin's coherence decays as a Gaussian depending only on the hyperfine interaction parallel to the field's direction. Our results agree with a central-spin

model for the electron and hole encompassing the Zeeman and hyperfine interactions. Our comprehensive study is an important step towards bringing quantum-dot-based sources of indistinguishable and entangled photons closer to real applications.

The support of the Israeli Science Foundation (ISF) (Grant No. 3756-20), and that of the European Research Council (ERC) under the European Union's Horizon 2020 research and innovation programme (Grant Agreement No. 695188) are gratefully acknowledged.

- [1] J. P. Reithmaier, G. Şek, A. Söfler, C. Hofmann, S. Kuhn, S. Reitzenstein, L. V. Keldysh, V. D. Kulakovskii, T. L. Reinecke, and A. Forchel, *Nature (London)* **432**, 197 (2004).
- [2] T. Yoshie, A. Scherer, J. Hendrickson, G. Khitrova, H. M. Gibbs, G. Rupper, C. Ell, O. B. Shchekin, and D. G. Deppe, *Nature (London)* **432**, 200 (2004).
- [3] M. Arcari, I. Söllner, A. Javadi, S. Lindskov Hansen, S. Mahmoodian, J. Liu, H. Thyrrestrup, E. H. Lee, J. D. Song, S. Stobbe, and P. Lodahl, *Phys. Rev. Lett.* **113**, 093603 (2014).
- [4] P. Senellart, G. Solomon, and A. White, *Nat. Nanotechnol.* **12**, 1026 (2017).
- [5] D. Najer, I. Söllner, P. Sekatski, V. Dolique, M. C. Söbl, D. Riedel, R. Schott, S. Starosielec, S. R. Valentin, A. D. Wieck, N. Sangouard, A. Ludwig, and R. J. Warburton, *Nature (London)* **575**, 622 (2019).
- [6] N. Somaschi, V. Giesz, L. D. Santis, J. C. Loredó, M. P. Almeida, G. Hornecker, S. L. Portalupi, T. Grange, C. Antón, J. Demory, C. Gómez, I. Sagnes, N. D. Lanzillotti-Kimura, A. Lemaître, A. Auffeves, A. G. White, L. Lancio, and P. Senellart, *Nat. Photonics* **10**, 340 (2016).
- [7] A. V. Kuhlmann, J. Houel, A. Ludwig, L. Greuter, D. Reuter, A. D. Wieck, M. Poggio, and R. J. Warburton, *Nat. Phys.* **9**, 570 (2013).
- [8] X. Ding, Y. He, Z.-C. Duan, N. Gregersen, M.-C. Chen, S. Unsleber, S. Maier, C. Schneider, M. Kamp, S. Höfling, C.-Y. Lu, and J.-W. Pan, *Phys. Rev. Lett.* **116**, 020401 (2016).
- [9] O. Benson, C. Santori, M. Pelton, and Y. Yamamoto, *Phys. Rev. Lett.* **84**, 2513 (2000).
- [10] N. Akopian, N. H. Lindner, E. Poem, Y. Berlatzky, J. Avron, D. Gershoni, B. D. Gerardot, and P. M. Petroff, *Phys. Rev. Lett.* **96**, 130501 (2006).
- [11] W. B. Gao, P. Fallahi, E. Togan, J. Miguel-Sanchez, and A. Imamoglu, *Nature (London)* **491**, 426 (2012).
- [12] K. De Greve, L. Yu, P. L. McMahon, J. S. Pelc, C. M. Natarajan, N. Y. Kim, E. Abe, S. Maier, C. Schneider, M. Kamp, S. Höfling, R. H. Hadfield, A. Forchel, M. M. Fejer, and Y. Yamamoto, *Nature (London)* **491**, 421 (2012).
- [13] J. R. Schaibley, A. P. Burgers, G. A. McCracken, L.-M. Duan, P. R. Berman, D. G. Steel, A. S. Bracker, D. Gammon, and L. J. Sham, *Phys. Rev. Lett.* **110**, 167401 (2013).
- [14] Z. Luo, S. Sun, A. Karasahin, A. S. Bracker, S. G. Carter, M. K. Yakes, D. Gammon, and E. Waks, *Nano Lett.* **19**, 7072 (2019).
- [15] N. H. Lindner and T. Rudolph, *Phys. Rev. Lett.* **103**, 113602 (2009).
- [16] S. E. Economou, N. Lindner, and T. Rudolph, *Phys. Rev. Lett.* **105**, 093601 (2010).
- [17] I. Schwartz, D. Cogan, E. R. Schmidgall, Y. Don, L. Gantz, O. Kenneth, N. H. Lindner, and D. Gershoni, *Science* **354**, 434 (2016).
- [18] D. Cogan, Z.-E. Su, O. Kenneth, and D. Gershoni, [arXiv:2110.05908](https://arxiv.org/abs/2110.05908).
- [19] M. Zwerger, W. Dür, and H. J. Briegel, *Phys. Rev. A* **85**, 062326 (2012).
- [20] W. J. Munro, A. M. Stephens, S. J. Devitt, K. A. Harrison, and K. Nemoto, *Nat. Photonics* **6**, 777 (2012).
- [21] K. Azuma, K. Tamaki, and H.-K. Lo, *Nat. Commun.* **6**, 6787 (2015).
- [22] D. Buterakos, E. Barnes, and S. E. Economou, *Phys. Rev. X* **7**, 041023 (2017).
- [23] M. Bayer, G. Ortner, O. Stern, A. Kuther, A. A. Gorbunov, A. Forchel, P. Hawrylak, S. Fafard, K. Hinzer, T. L. Reinecke, S. N. Walck, J. P. Reithmaier, F. Klopff, and F. Schäfer, *Phys. Rev. B* **65**, 195315 (2002).
- [24] D. Gammon, A. L. Efros, T. A. Kennedy, M. Rosen, D. S. Katzer, D. Park, S. W. Brown, V. L. Korenev, and I. A. Merkulov, *Phys. Rev. Lett.* **86**, 5176 (2001).
- [25] I. A. Merkulov, A. L. Efros, and M. Rosen, *Phys. Rev. B* **65**, 205309 (2002).
- [26] A. V. Khaetskii, D. Loss, and L. Glazman, *Phys. Rev. Lett.* **88**, 186802 (2002).
- [27] J. Fischer, W. A. Coish, D. V. Bulaev, and D. Loss, *Phys. Rev. B* **78**, 155329 (2008).
- [28] D. Cogan, O. Kenneth, N. H. Lindner, G. Peniakov, C. Hopfmann, D. Dalacu, P. J. Poole, P. Hawrylak, and D. Gershoni, *Phys. Rev. X* **8**, 041050 (2018).
- [29] See Supplemental Material at <http://link.aps.org/supplemental/10.1103/PhysRevB.105.L041407> for the central-spin model describing the evolution of a quantum dot electronic spin in the presence of an externally applied magnetic field and the nuclear spins in the quantum dot.
- [30] H. Bluhm, S. Foletti, I. Neder, M. Rudner, D. Mahalu, V. Umansky, and A. Yacoby, *Nat. Phys.* **7**, 109 (2011).
- [31] P.-F. Braun, X. Marie, L. Lombez, B. Urbaszek, T. Amand, P. Renucci, V. K. Kalevich, K. V. Kavokin, O. Krebs, P. Voisin, and Y. Masumoto, *Phys. Rev. Lett.* **94**, 116601 (2005).
- [32] B. D. Gerardot, D. Brunner, P. A. Dalgarno, P. Öhberg, S. Seidl, M. Kroner, K. Karrai, N. G. Stoltz, P. M. Petroff, and R. J. Warburton, *Nature (London)* **451**, 441 (2008).
- [33] D. Brunner, B. D. Gerardot, P. A. Dalgarno, G. Wüst, K. Karrai, N. G. Stoltz, P. M. Petroff, and R. J. Warburton, *Science* **325**, 70 (2009).
- [34] B. Eble, C. Testelin, P. Desfonds, F. Bernardot, A. Balocchi, T. Amand, A. Miard, A. Lemaître, X. Marie, and M. Chamarro, *Phys. Rev. Lett.* **102**, 146601 (2009).
- [35] F. Fras, B. Eble, P. Desfonds, F. Bernardot, C. Testelin, M. Chamarro, A. Miard, and A. Lemaître, *Phys. Rev. B* **84**, 125431 (2011).
- [36] K. De Greve, P. L. McMahon, D. Press, T. D. Ladd, D. Bisping, C. Schneider, M. Kamp, L. Worschech, S. Höfling, A. Forchel, and Y. Yamamoto, *Nat. Phys.* **7**, 872 (2011).
- [37] Y. Li, N. Sinitsyn, D. L. Smith, D. Reuter, A. D. Wieck, D. R. Yakovlev, M. Bayer, and S. A. Crooker, *Phys. Rev. Lett.* **108**, 186603 (2012).

- [38] J. H. Prechtel, A. V. Kuhlmann, J. Houel, A. Ludwig, S. R. Valentin, A. D. Wieck, and R. J. Warburton, *Nat. Mater.* **15**, 981 (2016).
- [39] A. Bechtold, D. Rauch, F. Li, T. Simmet, P.-L. Ardel, A. Regler, K. Muller, N. A. Sinitsyn, and J. J. Finley, *Nat. Phys.* **11**, 1005 (2015).
- [40] D. Cogan, G. Peniakov, Z.-E. Su, and D. Gershoni, *Phys. Rev. B* **101**, 035424 (2020).
- [41] Y. Benny, Y. Kodriano, E. Poem, D. Gershoni, T. A. Truong, and P. M. Petroff, *Phys. Rev. B* **86**, 085306 (2012).
- [42] S. Hameau, Y. Guldner, O. Verzelen, R. Ferreira, G. Bastard, J. Zeman, A. Lemaître, and J. M. Gérard, *Phys. Rev. Lett.* **83**, 4152 (1999).
- [43] W. D. Knight, *Phys. Rev.* **76**, 1259 (1949).
- [44] A. W. Overhauser, *Phys. Rev.* **92**, 411 (1953).
- [45] E. Barnes and S. E. Economou, *Phys. Rev. Lett.* **107**, 047601 (2011).
- [46] S. G. Carter, S. E. Economou, A. Greilich, E. Barnes, T. Sweeney, A. S. Bracker, and D. Gammon, *Phys. Rev. B* **89**, 075316 (2014).